Broadband-infrared assessment of phonon resonance in scattering-type near-field microscopy

S. Amarie and F. Keilmann*

Max Planck Institute of Quantum Optics and Center for NanoScience, Am Coulombwall 1, D-85714 Garching, Germany

(Received 16 May 2010; revised manuscript received 22 November 2010; published 20 January 2011)

The phonon-enhanced near-field response of polar materials is studied in theory and with a broadband midinfrared near-field microscope that generates spectra in real time. *Absolute* magnitude and phase spectra are determined for SiC, SiO_2, and *a*-SiO_2 at several demodulation orders. The data set is compared with results from two theoretical models of near-field interaction, point dipole and finite dipole. Only the latter produces acceptable agreement *with a single parameter choice* of all measured quantities (line shape in amplitude and phase, line position, and absolute scattering amplitude). This allows determining for the commercial metal tip used that (i) the dipole representing the near-field interaction has 600-nm effective length and that (ii) its near-field-induced far-field backscattering amplitude efficiency reaches 0.3% at phonon resonance, for the NA $\approx$ 0.45 objective used. The near-field phonon resonance is a robust and well-understood feature whose bright and sharp ($Q \approx 200$) signatures specifically can highlight and can identify polar materials in the nanoscale imaging of heterogeneous composites.

DOI: 10.1103/PhysRevB.83.045404 PACS number(s): 78.20.Ci, 42.72.Ai, 63.20.D−, 68.37.Uv

I. INTRODUCTION

Electromagnetic fields are intensified near tips and other sharply curved interfaces. A further effect is that elastic or inelastic light scattering from such structures is also enhanced.[1] Both effects can become augmented by intrinsic dielectric resonance of either the tip's material or that of a close-by sample. Such a dielectric resonance occurs in conductors due to mobile charge carriers (plasmonic enhancement) or in polar crystalline or amorphous matter due to bond vibrations (phononic enhancement). A well-known consequence is the enhanced Raman scattering observed on a rough metallic surface [surface-enhanced Raman scattering (SERS)] or from a metal tip (tip-enhanced Raman scattering).[2] Less well known is the enhanced Rayleigh scattering induced by dielectric resonance in scattering-type near-field optical microscopy (s-SNOM),[3] as first observed with phononic enhancement in SiC.[4]

The possibility of achieving great subwavelength optical resolution through near-field effects had been suggested very long ago[5] and was realized about 15 years ago both in the visible and the microwave regions, at $\lambda/1000$ (Ref. 6) and $\lambda/1\,000\,000$ (Ref. 7) spatial resolution, respectively (for a review, see Ref. 3). Present s-SNOMs employ an atomic force microscope (AFM) as a base instrument, detect the tip-scattered radiation with an interferometric receiver for enhanced signal-to-noise (S/N) ratio, and, for phase contrast, periodically dither the tip-sample distance to modulate the degree of near-field interaction and demodulate the detector signal at typically the second or third harmonic to suppress the strong yet very weakly modulated background scattering from higher up the tip shaft. S-SNOMs successfully map complex-valued material contrast, analyze complex-valued optical field patterns of plasmonic particles, and, with *step-tuned lasers*, determine near-field spectra of, e.g., individual virus or within crystal strain fields.[3] As a much-desired alternative for acquiring near-field spectra, the method of *supercontinuum beam illumination* was introduced,[8–10] the improved version of which enables the spectroscopic study provided in this paper.

Dielectrically resonant near-field interaction was first described with an electrostatic model developed to describe the SERS effect.[1] An adaptation of this model could explain s-SNOM contrast[11] and was subsequently further developed for this purpose.[12] In this paper, Sec. II gives the theoretical concept by casting two previously established models into a consistent form, including proximity scattering effects. Quantitative s-SNOM spectra are predicted for the near-field phonon resonance of distinct materials and for distinct parameter variations to be tested by experiment. Section III describes a new broadband infrared source based on a <100-fs fiber laser that is employed to operate a commercial s-SNOM for recording continuous spectra at ~20-nm spatial resolution. Quantitative complex near-field spectra in the range of 700–1400 cm^{-1} are measured for several crystalline and amorphous polar materials. Section IV discusses the results obtained in comparison with the model predictions. Conclusions are drawn on the reliability, specificity, and sensitivity of using phonon resonance as a tool to highlight desired materials in near-field microscopy.

II. THEORY

The theoretical description of light scattering from a sharply pointed probe tip requires the joint consideration of both radiative and nonradiative aspects. Antenna theory[13] deals with radiative coupling to charges in a given structure and allows for predicting its radiation resistance, its antenna length, and its far-field angular pattern (antenna lobes) but not its near-field distribution. In the context of s-SNOM, only one numerical study has treated both far and near fields, considering both the large scales of a real tip (20 μm) and of the wavelength (10 μm), simultaneously with the fine scale of the tip apex region (10 nm).[14] It suggested that an s-SNOM's far-field pattern depends strongly on the presence of a sample and on the sample's dielectric value.

Nonradiative near-field interaction between tip and sample in the electrostatic limit has been modeled analytically. It predicts an effective polarizability α_{eff} of the tip-sample

system. Assuming it is proportional to the complex far-field scattering efficiency σ of the tip-sample system[15]

$$\sigma = se^{i\varphi} = E_s/E_i \propto \alpha_{\text{eff}}, \tag{1}$$

where E_i and E_s are the incident and scattered far fields, respectively, one has a practical means of predicting *relative* contrast in s-SNOM.[3] As our experiment (Sec. III) determines *absolute* scattering efficiency, we extend Eq. (1) to read

$$\sigma = se^{i\varphi} = E_s/E_i = \left(1 + \sum_0^n p_i\right)^2 \frac{\alpha_{\text{eff}}}{V}, \tag{2}$$

where V is a complex volume to be determined experimentally and p_i are complex coefficients of proximity scattering by individual proximal scatterers i. As to the latter, let us define any object within the illuminated region around the tip as a proximal scatterer. The proximally scattered fields add coherently to the direct field at the tip, as is expressed in the parentheses of Eq. (2). This factor appears squared because, by reciprocity, the proximity scatterers also provide additional light paths for the observation of the tip's scattering. The focal spot diameter may be as small as about one wavelength across in the case of a strongly focused optical system but also much larger otherwise. Clearly proximal scattering provides extra terms through which a sample's properties enter into the s-SNOM signal.[16] Specific proximal scatterers were studied earlier in the mapping of eigenfield distributions near plasmon-resonant small particles[17] and antenna structures[18] and in the mapping of propagating surface phonon polaritons launched from inhomogeneities and antennas on the sample surface.[19]

The samples investigated in Sec. IV are flat and homogeneous. Still, one term of proximal scattering p_0 remains. It originates from the sample surface whose reflection provides an additional illumination of the tip. Using $p_0 = r_p$, the far-field Fresnel reflection coefficient for p-polarized incidence[12,16] (following the assumption that only z-oriented fields induce currents in a thin z-oriented wire), Eq. (2) becomes

$$\sigma = se^{i\varphi} = E_s/E_i = (1 + r_p)^2 \frac{\alpha_{\text{eff}}}{V}. \tag{3}$$

To describe measurable s-SNOM signals, we take account of the common technique of mechanically modulating the tip-sample distance z at the cantilever's resonance frequency Ω at a small amplitude Δz. Thus, the scattering efficiency is a time series,

$$\sigma(t) = \sigma_0 + \sigma_1 \cos \Omega t + \sigma_2 \cos 2\Omega t + \cdots. \tag{4}$$

The experiment determines one or more harmonic components of the detector signal. For $n \geqslant 2$ or 3, these usually represent the near-field scattering free of unwanted background scattering (mostly Rayleigh scattering from higher up the tip shaft or from sample inhomogeneities).[3] Accordingly, theory has to predict the corresponding Fourier coefficients $\alpha_{\text{eff},n}$ by taking explicit account of the dependence of α_{eff} on the tip-sample distance z.

For this purpose, we evaluate electrostatic models of near-field interaction in two versions of increasing refinement, the point-dipole (PD) model[20] and the finite-dipole (FD) model.[12] Both concepts are illustrated in Fig. 1. They reduce the real tip

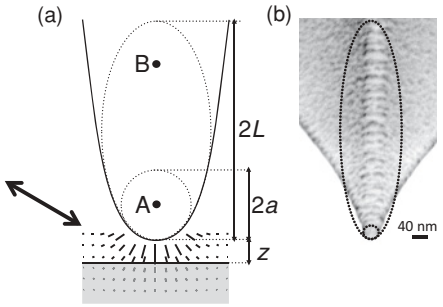

FIG. 1. Sketches (a) of two theoretical concepts of s-SNOM and (b) of corresponding interaction regions (dotted) overlaid on the SEM image of the experimentally used probe, which has a 40-nm tip diameter. The tip-enhanced optical field (vector pattern) polarizing the sample (gray) is confined below the apex to a dimension of the tip radius a. The field originates in the PD model from a PD at A oriented along the tip axis and in the FD model from a point charge near A that is neutralized by a countercharge at B. The double arrow indicates the incident and the Rayleigh-scattered beams for the experimental back-scattering geometry at 60° incidence.

structure either to a sphere or to a spheroid, dotted, respectively, that is polarized by the incident field. The near field in the apex region is approximated in the PD model by the field of a PD having the sphere's polarizability and being located in the sphere's center (A). The FD model considers the near field to result from a point charge located near A; this charge is thought to result from the incident field polarizing a spheroid of length $2L$ (Fig. 1) thereby inducing a countercharge near B. Both models treat image charges induced in the sample half-space characterized by a dielectric value $\varepsilon = \varepsilon_1 + i\varepsilon_2$, which, in turn, induce image charges in the tip.[1,2]

The PD model uses the well-known polarizability of a sphere of the tip's material with radius a and dielectric value ε_t,[13]

$$\alpha = 4\pi a^3 \frac{\varepsilon_t - 1}{\varepsilon_t + 2}. \tag{5}$$

This value is assigned to the PD oriented along the tip axis (for the same reason stated previously that only z-oriented fields induce currents in a thin z-oriented wire). For the half-space sample with dielectric value ε located at distance z below the tip apex, the PD model predicts

$$\alpha_{\text{eff}} = \frac{\alpha}{1 - \frac{\alpha\beta}{16\pi(a+z)^3}}, \tag{6}$$

where the abbreviation

$$\beta = \frac{\varepsilon - 1}{\varepsilon + 1} \tag{7}$$

defines the surface response function of the sample. Figure 2(a) shows our results for SiC. The dielectric function was assumed to represent a single-phonon oscillator (characterized by a longitudinal optical phonon frequency ω_{LO}, a transverse optical phonon frequency ω_{TO}, and a damping rate Γ) and a Drude relaxator (characterized by a plasma frequency ω_p and a damping rate γ),

$$\varepsilon_s(\omega) = \varepsilon_\infty \left(1 + \frac{\omega_{LO}^2 - \omega_{TO}^2}{\omega_{TO}^2 - \omega^2 - i\omega\Gamma} + \frac{\omega_p^2}{-\omega^2 - i\omega\gamma}\right), \tag{8}$$

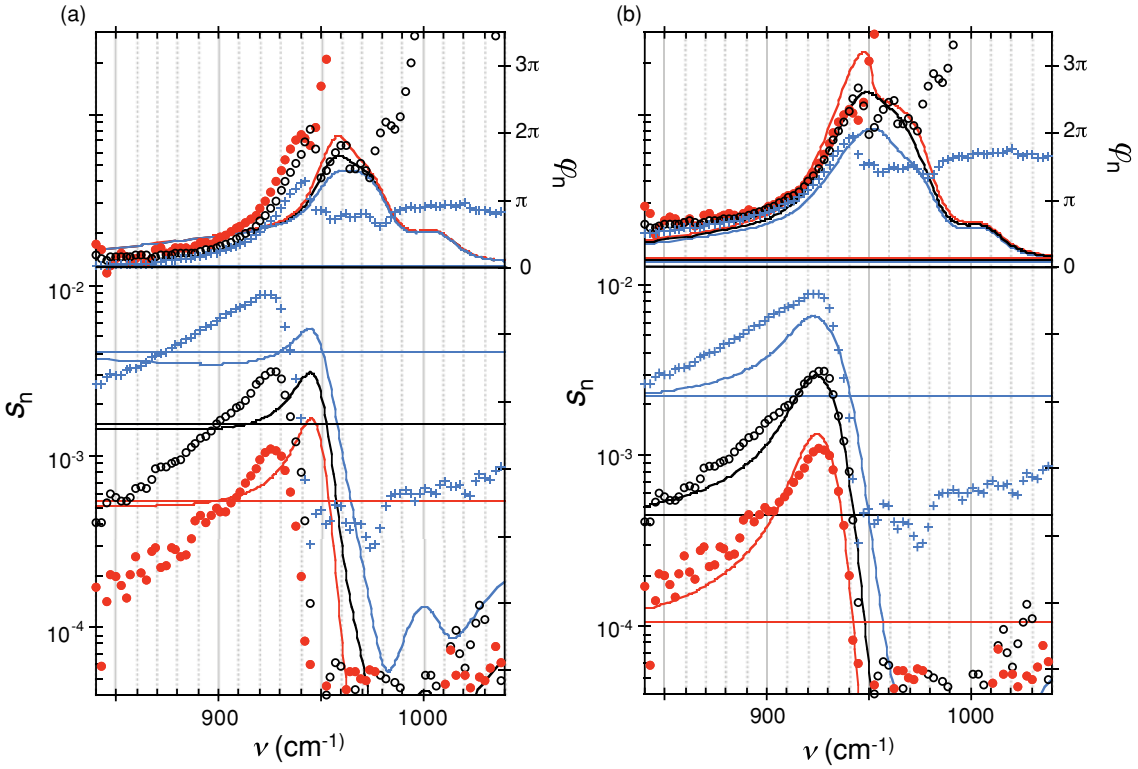

FIG. 2. (Color online) Theoretical predictions (curves) of scattering amplitude spectra s_n (lower parts) and phase spectra φ_n (upper parts) of a flat sample of either SiC or Au [for $n = 1$ (blue), 2 (black), and 3 (red)]; the SiC spectra show the phonon resonance while the Au spectra are flat; assumed tip material Pt, curvature radius $a = 20$ nm, and tapping amplitude $\Delta z = 10$ nm; (a) PD model with Re $(V) = (190\ \text{nm})^3$, (b) FD model with Re $(V) = (700\ \text{nm})^3$, $2L = 600$ nm, and Re $(g) = 0.7$. For the experimental data (points), see Sec. IV.

with the parameters $\omega_{LO} = 971\ \text{cm}^{-1}$, $\omega_{TO} = 797\ \text{cm}^{-1}$, $\varepsilon_\infty = 6.56$, $\Gamma = 6.6\ \text{cm}^{-1}$, $\omega_p = 275\ \text{cm}^{-1}$, and $\gamma = 450\ \text{cm}^{-1}$.[21] A tip radius $a = 20$ nm and a tapping amplitude $\Delta z = 10$ nm were chosen. The angle of incidence was set to 60° from the normal, and backscattering was assumed as symbolized by the double arrow in Fig. 1(a). Lastly, Re $(V) = (190\ \text{nm})^3$ was chosen to match the peak value of s_2 with the experimental data (see Sec. IV).

The FD model has been derived in detail in Refs. 12 and 21. It assumes that the charges are distributed through a spheroid, and this distribution depends on the tip-sample distance z. Only a fraction of the charges contributes to the near-field interaction.[22] This fraction has been calculated to be $g = (0.7 \pm 0.1)\,\text{e}^{0.08ui}$.[21] The analytic prediction is

$$\alpha_{\text{eff}} = a^2 L \frac{L(\varepsilon_t - 1)\left(2L\sqrt{1-a/L} + a\ln\frac{\left(1-\sqrt{1-a/L}\right)^2}{a/L}\right)}{2L\sqrt{1-a/L}\left((L-a\varepsilon_t) - aL(\varepsilon_t-1)\ln\frac{\left(1-\sqrt{1-a/L}\right)^2}{a/L}\right)}\left(2 + \frac{(gL-a-z)\beta\ln\frac{L}{z+3a/4}}{(z-gL+3a/4)\beta\ln\frac{L}{z+a/2}} + L\ln\frac{L}{a/4}\right). \quad (9)$$

This equation is the generalized form of Eq. (13) of Ref. 12 where ε_t was assumed infinite for a perfectly conducting spheroid; our generalization involved the use of Eq. (5.7) instead of Eq. (5.27) of Ref. 21.

Equation (9) contains, as a leading factor, the volume a^2L related to the assumed tip dipole [compare to a^3 in the corresponding Eq. (2) of the PD model]. The second factor [taken from Eq. (4.4) in Ref. 21] contains ε_t and has the meaning of a field-enhancement factor.[21] The third factor contains ε of the sample via the surface response function β [Eq. (7)] and describes the tip-dipole/image-dipole interaction.[12] Inserting Eq. (9) into Eq. (3), we proceed as in the PD model calculation to find the FD model results in Fig. 2(b). The extra parameters were set at $2L = 600$ nm and $g = 0.7e^{0.08i}$; a different value Re $(V) = (700\ \text{nm})^{-3}$ had to be chosen to match the peak value of s_2 with the experimental data.

III. A COHERENT BROAD-BAND INFRARED SOURCE FOR S-SNOM

Previous s-SNOM work has mostly used fixed-wavelength illumination in the visible, midinfrared, or terahertz regions. Continuous or stepwise tuning of laser lines has allowed for the determination of s-SNOM spectral contrast from phonons, molecular fingerprint vibrations, and conduction phenomena.[3] This approach generates spectra by repeated s-SNOM imaging at varied wavelengths. Sequential imaging is, however, problematic because of irreproducibilities caused by tip erosion or debris pickup and by sample drift. The alternative approach of determining complete spectra at each scanned pixel has been realized in the terahertz[9] and midinfrared[8,10,14] regions. Unfortunately, the available beam power in these experiments stayed by 3 to 4 orders of magnitude below the 10-mW level that is ideal for s-SNOM. The attained signal level did not suffice to acquire near-field spectra in less than 10 s and, thus, precluded an optimal focus alignment based on the near-field response as well as the mapping of a sample.

In order to generate a strong midinfrared supercontinuum coherent beam, we use infrared difference-frequency generation in GaSe by superimposing two pulse trains emitted from a mode-locked Er-doped fiber laser (model FFS.SYS-2B with FFS-CONT of toptica.com). In this system, two internal Er fiber amplifiers deliver separate beams of 250-mW average power each, in <100-fs pulses centered at 1.55 μm at 88-MHz repetition rate. One of the beams passes an internal nonlinear fiber to acquire a supercontinuum (SC) spectrum, which can be tuned in the 0.9–2.2-μm range by internal prisms. Here, we use the long-wavelength part of the SC for difference-frequency mixing with the Er laser beam at 1.55 μm as demonstrated before.[23]

Our setup is sketched in Fig. 3. The SC beam is polarized vertically and collimated to 6-mm diameter using CaF_2 lenses L1 and L2 of 25- and 200-mm focal lengths, respectively. The Er laser beam is horizontally polarized and is transformed into a collimated elliptical shape, 6-mm vertical and 2-mm horizontal, by using the lens L3 at 50 mm focal length (fL), and two cylindrical lenses CYL1 and CYL2 at 50 and 150 mm fL, respectively. Both beams are collinearly combined by a custom dichroic reflector at 45° incidence (BC from ultrafast-innovations.com). The temporal and spatial overlaps of both pulse trains is verified (not shown) by temporarily

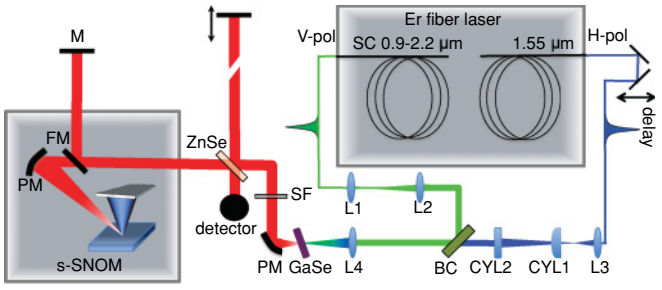

FIG. 3. (Color online) Optical layout of a coherent broadband midinfrared source based on frequency-difference generation in GaSe illuminating an s-SNOM via a Michelson interferometer.

inserting a low-pass filter (FEL 1450 from thorlabs.com) in order to suppress the high-frequency part of the SC and by focusing the combined beams at 10 cm fL to a photodetector (model 1621 from newfocus.com), which, for this spectral range, responds to two-photon processes only, thus, signalizing pulse overlap. Adjustment of the Er laser beam path length is carried out by a delay stage (an SC pulse leaves the laser box ~300 ps later than the Er laser pulse). A 100-mm fL CaF_2 lens L4 focuses the combined beams onto a z-oriented GaSe crystal (from nlo-crystal.tomsk.ru) at 30°–40° off normal as depicted, depending on the desired wavelength region. The SC and Er laser powers incident on the crystal are 15 and 160 mW, respectively. The crystal's c axis is rotated 45° from horizontal. A 1-mm crystal thickness is chosen for maximum parametric gain.[23]

The generated midinfrared beam is collimated using a 50-mm fL off-axis parabolic mirror (PM) to a beam diameter of ~11 mm. The polarization is vertical. When tuned to ~10-μm wavelength, the power is up to 25 μW, less than reported in Ref. 23, as measured with a thermopile and corrected for loss by an uncoated InAs wafer, which served as a 700–2700 cm^{-1} bandpass filter.

The midinfrared beam is passed through a low-pass scattering filter (SF) in order to avoid cantilever heating. For this, we use, as in a former work,[8] an NaCl plate at Brewster's angle, which has one surface roughened by slight sandblasting. A midinfrared transmittance of >95% was maintained, while roughness scattering heavily attenuated the beam's near-infrared components at 1.55- and 2-μm wavelengths.

The midinfrared beam then enters the home-built Michelson interferometer coupled to the commercial s-SNOM (NeaSNOM from neaspec.com) as recently described.[10] Briefly, an uncoated ZnSe plate is used for beam splitting and combining, together with an HgCdTe detector (KLD-0.25-J1 from kolmar.com) and a commercial cantilevered Pt-coated tip (NCPt-10 arrow from nanoworld.com). The NeaSNOM has two optical ports to accept 15-mm-diameter collimated input beams, which can be chosen in the visible, infrared, or terahertz region for optical imaging at 20-nm resolution. We use only one of the ports for backscattering operation. An internal electronics provides real-time topography and optical signals, the latter including amplitude and phase at several demodulation orders n simultaneously. An optimal alignment of the remotely controlled 20-mm fL internal PM is achieved in two steps. At first, the n = first demodulation-order interferogram is observed, at reduced interferogram length, and the free-induction decay feature[10] is maximized. Then, this procedure is repeated for the weaker n = second demodulation-order interferogram. Finally, the full interferogram length of 1.7 mm is scanned in 4 s, and 2–20 averages are taken before complex Fourier transformation. In order to relate the backscattered field amplitude to the incident field amplitude, a flip mirror FM is temporarily inserted in the sample arm of the interferometer so that the experimental spectra of tip backscattering can be normalized to those from the auxiliary mirror M. Thus, our technique enables the routine *absolute* determination of near-field-induced scattering.

IV. EXPERIMENTAL RESULTS AND DISCUSSION

Results of flat homogeneous samples of crystalline SiC and SiO_2 are shown in graphs combining theory and experiment (Figs. 2, 4–10). The experimental points are displayed for different demodulation orders in the same colors as the pertaining theory curves. For scaling the theoretical spectra, a matching was chosen for the experimental peak amplitude s_2 of SiC in Fig. 2. The chosen value of Re (V), defined in Eq. (2), was identically used for all theoretical spectra also of other materials in this paper.

Figure 2 demonstrates experimental near-field spectra of SiC in a quality not attained in earlier assessments.[3] This concerns the broad spectral coverage and the high S/N ratio even at the small tapping amplitude used, $\Delta z \approx a$. The amplitude resonance width is clearly seen to decrease with demodulation order n [after FD theory, 47-cm^{-1} full width at half maximum (FWHM) at $n = 1$, 30 cm^{-1} at $n = 2$, and 25 cm^{-1} at $n = 3$], a sharpening effect not experimentally observed before. It is also interesting that the resonance peak position stays constant at 925 cm^{-1} for different n's, within <5 cm^{-1}, which testifies to the robust potential of phonon signatures to identify materials.

Furthermore, it is noteworthy that even the s_1 spectrum has a similar shape to the s_2 and s_3 spectra, especially a steep edge at 935 cm^{-1}. This observation points to a nearly background-free measurement even in the first demodulation order, an achievement owed to the broadband interferograms. These develop long free-induction-decay signatures[10] through (phonon) resonance whose real-time observability guarantees a perfect alignment of the focusing optics. It is encouraging that an NA $\approx$ 0.45 optics, as used in the NeaSNOM, can indeed focus sharply enough to suppress unwanted scattering from higher up the tip shaft. Such background-free $n = 1$ operation of s-SNOM is highly desirable over the $n = 2$ operation because its three- to fivefold higher signal level allows an order-of-magnitude faster image acquisition, at equal S/N ratios.

Although, in principle, the phase possibly was not determined absolutely in the present paper because of thermal drifts of the interferometer arm lengths. The measured phase spectra displayed were obtained by selecting a white-light position off-line from the $n = 2$ interferograms, which was then also used for the $n = 1$ and $n = 3$ interferograms, the criterion being that—after Fourier transformation—the phase φ_2 matched the theoretical prediction on the low-frequency end of the spectrum. With this, the experimental results of both amplitude and phase spectra of SiC are in qualitative agreement with the line profiles measured in earlier works.[4,8,10,12,24,25]

The theory curves of Fig. 2(a) result from the PD model. The predicted resonance position comes out ~20 cm^{-1} higher than measured as noted before.[4,24] Another difference is that the ratio between peak amplitudes of consecutive demodulation orders is predicted to be 1.9, compared to 2.8 measured. Similarly, at the low-frequency side of the resonance at 875 cm^{-1}, this factor amounts to 2.7, compared to 4 measured.

The FD model [Fig. 2(b)], in contrast, matches the experiment much better as noted before.[12,25] Specifically, good agreement can be noted for the resonance position, for the shape of the amplitude resonance at low frequency, and for the amplitude ratio of consecutive demodulation orders. The FD model predicts the observed resonance sharpening with increasing n as does the PD model. Furthermore, we could experimentally verify (data not shown) the rather flat spectra predicted by the FD model for an Au sample, including a ratio ≈5 between the amplitudes of consecutive demodulation orders (in contrast to ≈3 after the PD model). Finally, also the phase spectra after the FD model agree satisfactorily with experiments in regions of sufficiently high and not too steeply changing amplitude. We conclude that the FD model—which, anyway, is more plausible as it pays tribute to the elongated tip form—is indeed the theoretical method of choice to explain the complex near-field scattering. It is used for all further calculations in this paper.

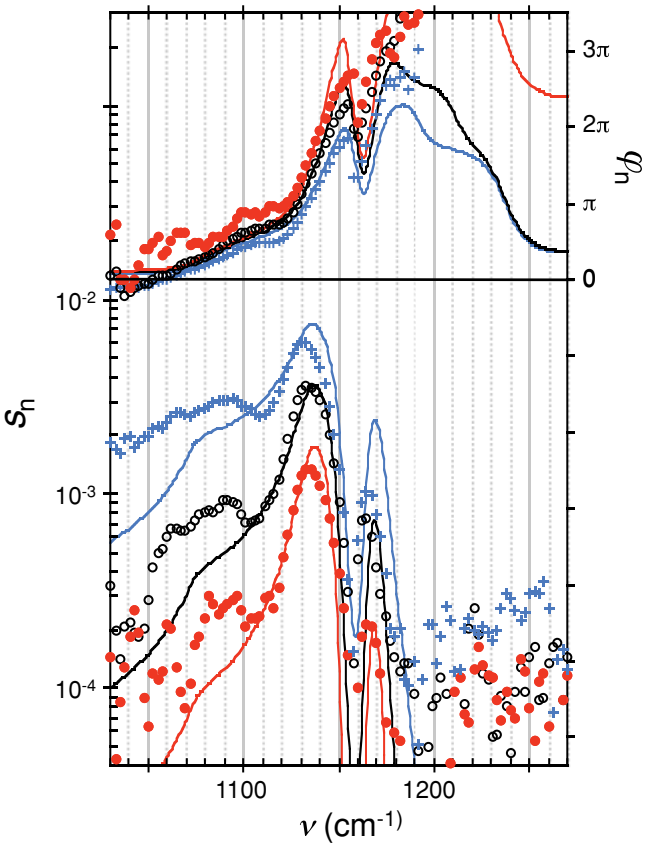

FIG. 4. (Color online) Experimental data and FD model predictions as in Fig. 2(b) of crystalline SiO_2; dielectric data from Table I.[26]

Quartz (SiO_2) has a more complex crystal structure, which supports several phonon modes and, thus, is investigated here to further help test the validity of s-SNOM theory. Results of its near-field response are shown in Fig. 4. A c-oriented sample was used for the experimental data displayed. The inspection microscope built in the NeaSNOM (resolution 0.7 μm) revealed some holes in the surface; the spectra were taken from locally flat regions. Two near-field resonances in close neighborhood are evident. They are due to two optical phonons known from infrared dispersion analysis[26] (Table I), which states that the higher-lying phonon couples to ordinarily but not to extraordinarily polarized light. Thus, this mode should not couple to light with the electric field polarized along

TABLE I. Dispersion parameters of quartz for the ordinary ray (o) and extraordinary ray (e) modified from Ref. 26.

	ω_{TO} (cm^{-1})		ω_{LO} (cm^{-1})		Γ (cm^{-1})	
ε_∞	o	e	o	e	o	e
o	1227	1220	1229	1223	135	183
2.356	1163		1165		7	
	1072	1080	1215	1222	7.6	7.5
	797	778	815	794	7.2	78
e	697	539	700	540	8.4	22
2.383		509		514		7.1
	450	495	522	559	4	4.5
	394	364	421	413	2.8	5.1

the c direction (optical axis). Surprisingly, we observe this higher mode even on the c-oriented surface, which suggests the near field is not strictly oriented parallel to the tip axis but contains a sizable transverse component. To test this, a Brazilian quartz crystal was polished as a cube with a-, b-, and c-oriented surfaces, and near-field spectra were taken of each surface (not shown). Interestingly, no difference could be seen among them. That the near field under a tip should have some transverse components is clear from inspecting the field distribution in Fig. 1(a), although the consequences for s-SNOM have not yet been addressed in the literature.—Somewhat outside this context, we note that, in s-SNOM, (i) the near-field polarization is not directly related to the incident far-field beam polarization, and (ii) the tip-induced near-field scattering strictly requires an incident far-field component along the tip axis as shown experimentally.[27]

The higher-lying quartz resonance has an experimental width of only 10 cm^{-1} (FWHM). The real width must be smaller because the instrumental resolution is 7 to 8 cm^{-1} (limited by 1.7-mm interferogram length and Hamming apodization). Accordingly, the real peak amplitude of this resonance must be larger. For the theoretical assessment, we use oscillator data from the cited analysis[26] and include all seven modes that couple to ordinary rays (Table I). The PD model produces (not shown) (i) resonance positions that are shifted to higher frequencies by ~20 cm^{-1} as in the SiC case, and (ii) a peak amplitude of the higher mode exceeding that of the lower mode. Much in contrast, a reasonable agreement with the experimental points is provided by the FD model calculations (Fig. 4). Here, identical values for Re (V), L, and g were used as in Fig. 2(b) (as also in further calculations in this paper). It is reassuring that the same value of the proportionality factor Re (V) applies to SiC and SiO_2, confirming that this factor indeed measures the far-field coupling, which, from its definition, should not be sample dependent. Some significant differences remain between theory and experiment, for example, a prominent, broad sideband around 1080 cm^{-1}, which is only weakly present in the theory result and a slight (5 cm^{-1}) redshift of the resonances.

With the example of crystalline SiO_2 (c-oriented surface), we examine several predictions of the FD model in detail, at first, the influence of the tapping amplitude on the near-field amplitude spectrum. One expects a monotonic rise at small

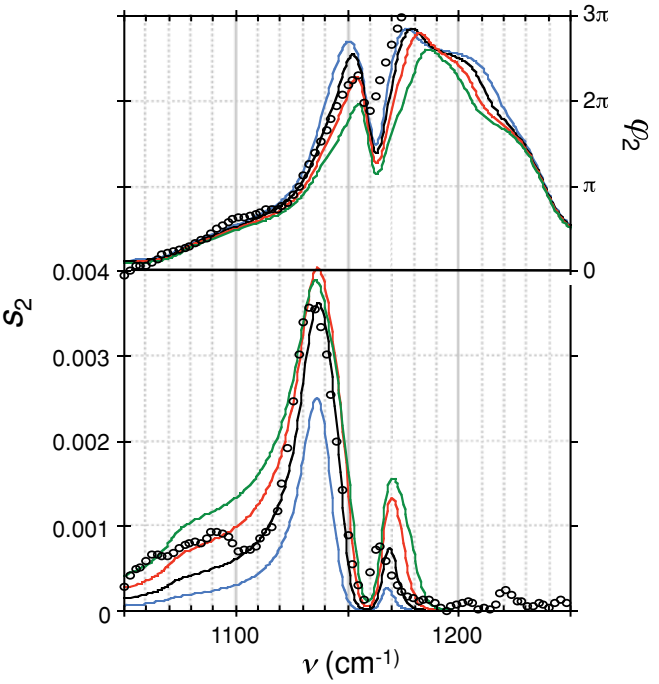

FIG. 5. (Color online) Experimental data and FD model predictions as in Fig. 4 of σ_2 of SiO_2 varying the tapping amplitude Δz = 5 nm (blue), 10 nm (black), 20 nm (red), and 40 nm (green).

amplitude, followed by saturation when Δz exceeds a, which is assumed to be 20 nm in this paper [see scanning electron microscopic (SEM) image in Fig. 1(b)]. This behavior is verified by the resulting spectra in Fig. 5, although verified differently for different features: The lower-lying mode's amplitude peak saturates already at $\Delta z = 20$ nm, whereas that of the higher-lying mode saturates around $\Delta z = 40$ nm and the sideband at 1080 cm^{-1} even higher. An important result from Fig. 5 is the robustness of the resonance position with respect to Δz, supporting the applicability of s-SNOM for material identification.

Second, a decisive experimental test of near-field interaction has been the strong near-field amplitude decrease on retracting the sample from the tip at a characteristic distance of about a.[28] Here, we demonstrate this behavior in the spectroscopic s-SNOM. Figure 6(a) shows the theoretically predicted 50% reduction of s_2 at $z \approx 6$ nm for the main resonance and $z \approx 20$ nm for the higher-lying resonance, respectively. The experiment [Fig. 6(b)] was carried out at a high tapping amplitude of $\Delta z = 40$ nm at low spectral resolution, in order to acquire the data in sufficiently short time (1 s per spectrum) to avoid thermal drift of the uncontrolled AFM. Nevertheless, the strong reduction of the amplitude is verified and even the distinctly longer decay length at the higher-lying resonance. The reason for this latter behavior probably is the inverse relation between the resonance strength and the spatial extent of the near-field region as borne out in a simulation.[28] The observed redshift of the resonance on a sample approach agrees with an earlier study of SiC.[24]

We also examine the influence of the parameter g, which had been derived to lie at about Re (g) = 0.7.[12] It turns out (Fig. 7) that its influence on the amplitude is more than

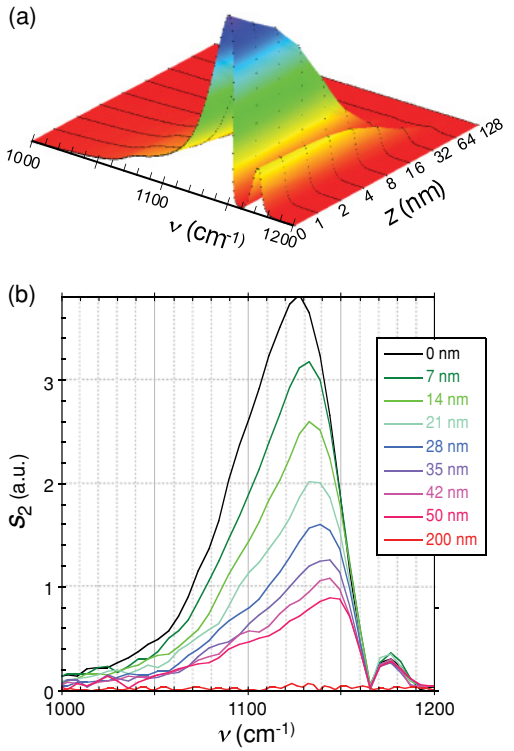

FIG. 6. (Color online) (a) Experimental data and FD model predictions as in Fig. 4 of s_2 of SiO_2 varying the distance z between the sample and the lower turning point of the oscillating tip as indicated.

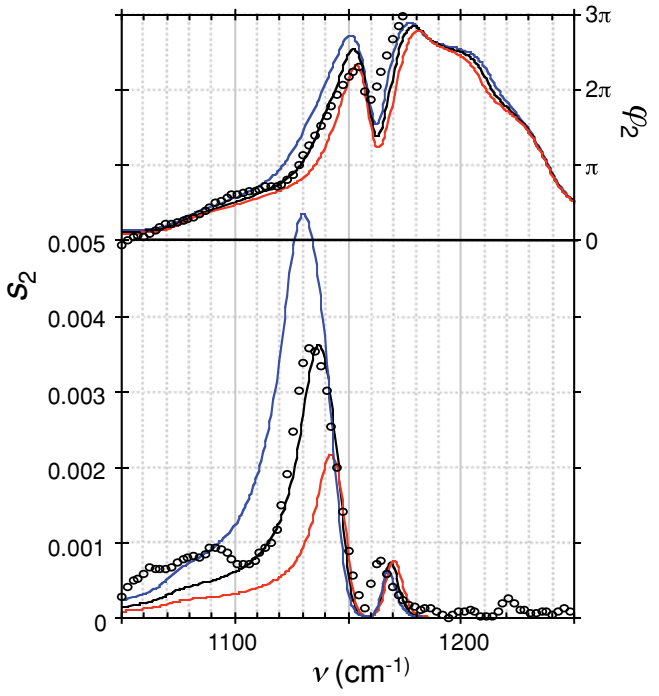

FIG. 7. (Color online) Experimental data and FD model predictions as in Fig. 4 of σ_2 of SiO_2 varying the fraction of mutual charge induction Re $(g) = 0.6$ (red), 0.7 (black), and 0.8 (blue).

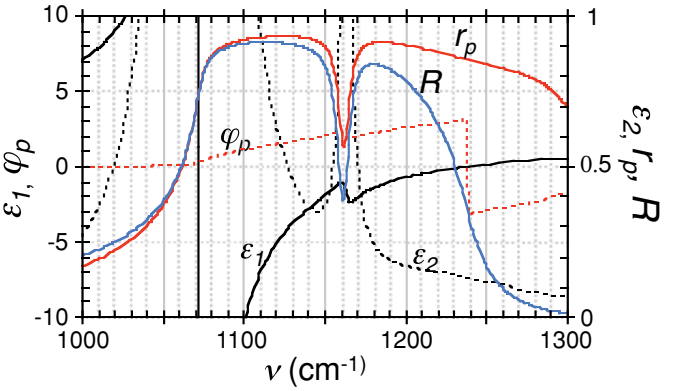

FIG. 8. (Color online) Calculated dielectric function ε (black), ε_1 (full), ε_2 (dotted) of crystalline SiO_2, Reststrahlen reflectivity R (blue), and Fresnel reflection (red), for 60° p-polarized incidence, amplitude (full), phase (dotted), after Table I.[26]

linear. Importantly, the value of Re (g) influences the resonance position. Judging from the lower-lying resonance, a choice of Re $(g) = 0.71$ instead of 0.7 would make up for the observed 5-cm^{-1} redshift of the resonance position. However, the effect is different with the higher-lying mode, which lets us keep Re $(g) = 0.7$ in all other calculations using the FD model.

At this point, it is instructive to consider the dielectric function of crystalline quartz (Fig. 8, for the ordinary ray). The transverse optical phonon frequencies can be read from the steep transitions in ε_1 to lie at 1072 and 1163 cm^{-1}.

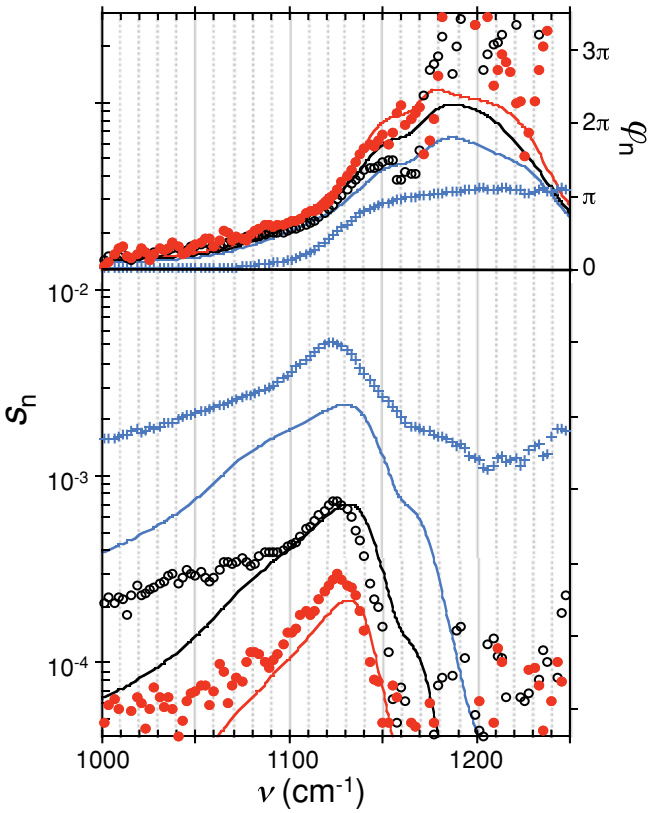

FIG. 9. (Color online) Experimental data and FD model predictions as in Fig. 2(b) of σ_2 of amorphous SiO_2 suprasil; dielectric data from Table I with all damping factors multiplied by 4.2.

The calculated Reststrahlen band (blue) is dominated by the stronger lower-lying resonance extending into the higher-lying resonance, which induces a dip at 1163 cm^{-1} by quantum interference. At the two positions of the experimental near-field resonances at 1133 (1164) cm^{-1} (Fig. 5), the dielectric behavior differs in several regards, namely, (i) a small (large) value of ε_2, (ii) a 90% (60%) Fresnel reflection amplitude r_p, and (iii) a value of ε_1 of -3 (-2). The latter difference illustrates that the near-field scattering is complex [Eqs. (3) and (9)] and certainly not a function of ε_1 alone. But detailed consequences are not drawn from Fig. 8 because the investigated crystal's dielectric function might slightly differ from that of Ref. 26 and should be verified with modern precision ellipsometry.

Finally, two types of amorphous SiO_2 were investigated. Figure 9 shows the result of a pure quartz glass (suprasil from schott.com), which clearly exhibits near-field phonon resonance, at about fourfold-reduced amplitudes s_2 and s_3 compared to crystalline quartz. The s_1 spectrum is relatively strong and seems dominated by background scattering. In the absence of a reliable dielectric function, we tentatively apply a dielectric function derived from that of crystalline quartz[26] but with increased damping rates Γ. With 4.2 times the Γ values of Table I, the FD model predicts near-field scattering spectra, which agree remarkably well with the experimental σ_2 and σ_3 resonances (Fig. 9).

A further glass sample investigated is tempax (borosilicate glass from schott.com). Figure 10 summarizes its measured σ_2 spectra, together with those of crystalline quartz and quartz glass for comparison. The scattering amplitude of tempax is smaller than that of quartz glass. The tempax spectra can be well described with FD theory, assuming an even higher damping of the phonon oscillators. The theory curves shown are based on multiplying the rates Γ of Table I by 8.2.

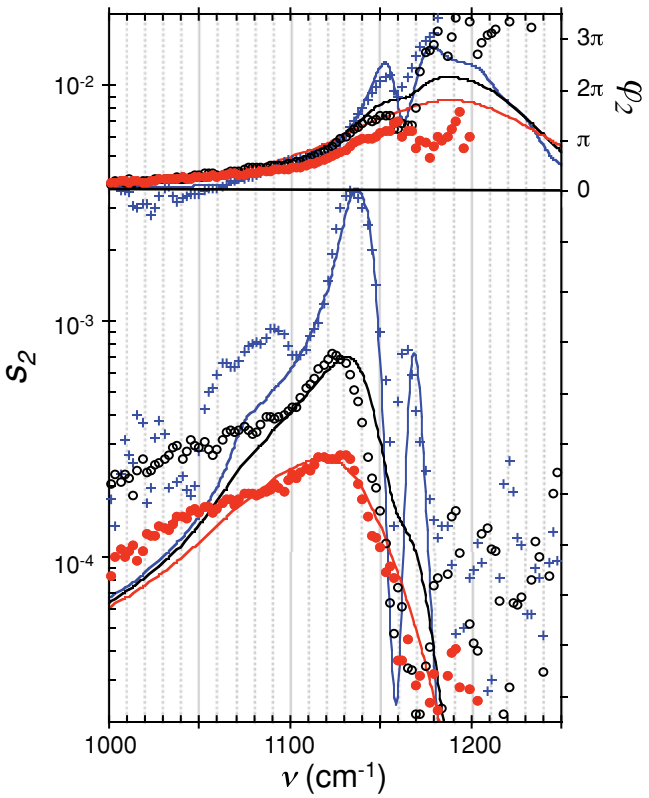

FIG. 10. (Color online) Experimental data and FD model predictions as in Fig. 2(b) of σ_2 comparing crystalline SiO_2 [(blue), from Fig. 4], amorphous SiO_2 suprasil [(black), from Fig. 9], and amorphous SiO_2 tempax [(red), dielectric data from Table I with all damping factors multiplied by 8.2].

V. CONCLUSIONS

The understanding of near-field interaction between tip and sample has been advanced by testing the FD theory in a detailed experiment with several phonon-resonant sample materials. The key technical improvement was the introduction of a sufficiently strong ($\approx$25 μW), stable, and broadband midinfrared coherent light source. This enabled the monitoring of interferograms of the near-field response in real time and, thus, a perfect focus alignment. Surprisingly, nearly background-free near-field spectra of phonon-resonant samples then become attainable even in the lowest (i.e., first) demodulation order.

The near-field phonon resonance of SiO_2 at 1164 cm^{-1} has been determined to be as sharp as 6 cm^{-1} (FWHM) by correcting the observed width of 10 cm^{-1} (FWHM) for the instrumental resolution of 7 cm^{-1}. The equivalent inverse relative linewidth $Q \approx 200$ underlines the high specificity by which the s-SNOM can recognize and can identify polar dielectric materials. The near-field phonon resonance is by more than an order of magnitude sharper than the corresponding far-field Reststrahlen reflection band, which is typically 100-cm^{-1} wide.

That phonon resonance may indeed become a preferred source of contrast in s-SNOM applications is also strongly suggested from its extraordinary signal strength: The absolute power efficiency of near-field backscattering of phonon-resonant materials exceeds that of an Au sample by about 50-fold in the case of polar crystals and still about 2.5-fold for a pure amorphous substance, such as a-SiO_2. Material-specific bright nanoscopic contrast suggests itself to the detection, chemical identification, and structural assignment of nanoscale crystals, for example, in the mineralogy of such diverse nanocomposites as found in extraterrestric dust or in biological hard matter.

The evidence has been strengthened that the FD model of near-field interaction—together with a proper consideration of proximity-illumination effects—can qualitatively account for the measured spectral shapes. An interesting outcome is that this matching requires an effectively 600-nm long dipole to represent the actual tip. Furthermore, a matching of the measured absolute near-field scattering efficiency requires the introduction of a reference volume of $(700\ nm)^3$. A clarification of the physical significance of both these quantities, however, has to await a future theory of near-field scattering that would combine both the far-field coupling and the near-field interaction in a unified description.

ACKNOWLEDGMENTS

The authors are indebted to M. Marangoni and A. Gambetta for their help in implementing the broadband infrared source. Advice and support by D. W. v. d. Weide,

V. Pervak, M. Betz, N. Ocelic, A. Huber, P. Weiser, and A. Apolonskiy is gratefully acknowledged. Thanks to a *Physical Review B* referee for valuabl advice on improving the text. Supported by Deutsche Forschungsgemeinschaft through the Cluster of Excellence Munich Centre for Advanced Photonics.

*fritz.keilmann@mpq.mpg.de

[1] P. K. Aravind and H. Metiu, Surf. Sci. **124**, 506 (1983).
[2] M. Moskovits, Rev. Mod. Phys. **57**, 783 (1985).
[3] F. Keilmann and R. Hillenbrand, in *Nano-Optics and Near-Field Optical Microscopy*, edited by A. Zayats and D. Richards (ArtechHouse, Norwood, MA, 2009).
[4] R. Hillenbrand, T. Taubner, and F. Keilmann, Nature (London) **418**, 159 (2002).
[5] E. H. Synge, Philos. Mag. **6**, 356 (1928).
[6] F. Zenhausern, Y. Martin, and H. K. Wickramasinghe, Science **269**, 1083 (1995).
[7] F. Keilmann, D. W. v. d. Weide, T. Eickelkamp, R. Merz, and D. Stöckle, Opt. Commun. **129**, 15 (1996).
[8] M. Brehm, A. Schliesser, and F. Keilmann, Opt. Express **14**, 11222 (2006).
[9] H. G. von Ribbeck, M. Brehm, D. W. Van Der Weide, S. Winnerl, O. Drachenko, M. Helm, and F. Keilmann, Opt. Express **16**, 3430 (2008).
[10] S. Amarie, T. Ganz, and F. Keilmann, Opt. Express **17**, 21794 (2009).
[11] B. Knoll and F. Keilmann, Nature (London) **399**, 134 (1999).
[12] A. Cvitkovic, N. Ocelic, and R. Hillenbrand, Opt. Express **15**, 8550 (2007).
[13] J. D. Jackson, *Classical Electrodynamics* (Wiley, New York, 1975).
[14] M. Brehm, A. Schliesser, F. Cajko, I. Tsuckerman, and F. Keilmann, Opt. Express **16**, 11203 (2008).
[15] C. F. Bohren and D. R. Huffmann, *Absorption and Scattering of Light by Small Particles* (Wiley-Interscience, New York, 1983).
[16] M. Brehm, Dissertation Technische Universität München (in German), 2006.
[17] R. Hillenbrand and F. Keilmann, Appl. Phys. B **73**, 239 (2001); R. Hillenbrand, F. Keilmann, P. Hanarp, D. S. Sutherland, and J. Aizpurua, Appl. Phys. Lett. **83**, 368 (2003).
[18] M. Schnell, A. García-Etxarri, A. J. Huber, K. Crozier, J. Aizpurua, and R. Hillenbrand, Nature Photon. **3**, 287 (2009).
[19] A. Huber, N. Ocelic, D. Kazentsev, and R. Hillenbrand, Appl. Phys. Lett. **87**, 81103 (2005); A. J. Huber, B. Deutsch, L. Novotny, and R. Hillenbrand, *ibid.* **92**, 203104 (2008).
[20] B. Knoll and F. Keilmann, Opt. Commun. **182**, 321 (2000).
[21] N. Ocelic, Dissertation Technische Universität, München, 2007.
[22] L.V. Lindell, G. Dassios, and K. I. Nikoskinen, J. Phys D **34**, 2302 (2001).
[23] A. Gambetta, R. Ramponi, and M. Marangoni, Opt. Lett. **33**, 2671 (2008).
[24] T. Taubner, F. Keilmann, and R. Hillenbrand, Nanoletters **4**, 1669 (2004).
[25] A. J. Huber, A. Ziegler, T. Köck, and R. Hillenbrand, Nat. Nanotechnol. **4**, 153 (2009).
[26] W. G. Spitzer and D. A. Kleinman, Phys. Rev. **121**, 1324 (1961).
[27] B. Knoll and F. Keilmann, J. Microsc. **194**, 512 (1999).
[28] J. Renger, S. Grafström, L. M. Eng, and R. Hillenbrand, Phys. Rev. B **71**, 075410 (2005).